Boosting magnetic resonance imaging signal-to-noise ratio using magnetic metamaterials

Guangwu Duan[1,#], **Xiaoguang Zhao**[1,#], **Stephan William Anderson**[2,*], **Xin Zhang**[1,*]

[1]Department of Mechanical Engineering and Photonics Center, Boston University, Boston, MA 02215, USA.

[2]Department of Radiology, Boston University Medical Campus, Boston, MA 02118, USA.

Abstract

Magnetic resonance imaging (MRI) represents a mainstay among the diagnostic imaging tools in modern healthcare. Signal-to-noise ratio (SNR) represents a fundamental performance metric of MRI, the improvement of which may be translated into increased image resolution or decreased scan time. Recently, efforts towards the application of metamaterials in MRI have reported improvements in SNR through their capacity to interact with electromagnetic radiation. While promising, the reported applications of metamaterials to MRI remain impractical and fail to realize the full potential of these unique materials. Here, we report the development of a magnetic metamaterial enabling a marked boost in radio frequency field strength, ultimately yielding a dramatic increase in the SNR (~ 4.2X) of MRI. The application of the reported magnetic metamaterials in MRI has the potential for rapid clinical translation, offering marked enhancements in SNR, image resolution, and scan efficiency, thereby leading to an evolution of this diagnostic tool.

Introduction

Magnetic resonance imaging (MRI) represents a powerful diagnostic tool in the armamentarium of modern healthcare that is widely applied across a spectrum of disease, from stroke to cancer imaging and beyond. When compared to alternative imaging modalities such as ultrasound (US) or computed tomography (CT), MRI offers the advantages of flexibility in generating image contrast from a range of tissue properties, leading to an inherently high degree of tissue contrast, as well as a lack of ionizing radiation. Chief among the performance metrics of MRI systems is the signal-to-noise ratio (SNR), which may be leveraged to boost overall acquisition performance, from image resolution to

the efficiency of image acquisition, and has been demonstrated to improve anatomic delineation and detection of pathology (1–5).

Over the past several decades, one of the fundamental methods by which to increase SNR in MRI has been through the development of platforms with increasingly powerful static magnetic fields (1.5 T, 3.0 T, and even 7.0 T clinical MRI systems). However, the trade-offs of this approach are significant, including increases in hardware costs, image artifacts, patient side effects, tissue heating, and implanted hardware and medical device safety concerns (6–9). In parallel, radiofrequency (RF) coil technology continues to improve and, currently, highly advanced multi-channel RF coils are routinely used in MRI (10, 11). In addition, a range of FDA-approved contrast agents, the majority of which are gadolinium-based, have been developed and are routinely employed in an effort to improve image quality and disease conspicuity. Finally, among other approaches, the ongoing design of sophisticated MRI pulse sequences and image-processing techniques yields further improvements in SNR, image quality, and overall scan efficiency (12).

Beyond the aforementioned conventional and commonly employed techniques, metamaterials have been applied in an effort to enhance MRI capabilities. Metamaterials represent a class of artificially structured materials, which may be engineered in order to exhibit properties not found in naturally occurring materials. Importantly, the unique properties of metamaterials are derived not only from the inherent properties of their constituent materials but also from the precise arrangement of their internal structure, yielding powerful design flexibility. Typically, metamaterials feature a composition of elements (termed unit cells), the size and spacing of which are sufficiently small compared to the spatial variation of the exciting field. Since they were originally theoretically described and, more recently, experimentally validated, metamaterials have drawn interest due to their unique properties such as negative refraction index, among others (13–15). With respect to MRI, the application of Swiss-roll and split-ring arrays has been demonstrated to improve MRI coil sensitivity, yielding improvements in SNR (16–18). Furthermore, magnetoinductive waveguides and flexible metamaterial endoscopes for MRI have also been reported to improve SNR and allow image transmission through a curved wire medium, respectively (19, 20). These early efforts at applying metamaterials to MRI, while promising, remain clinically impractical or, in some cases, superfluous or irrelevant to advancing modern MRI technology. More recently, a metasurface resonator has been reported to improve SNR in MRI using an ultrathin array of metallic wires (21). However, limitations of this approach include magnetic field inhomogeneity and the potential for generating strong electric fields, raising potential safety concerns.

Here, we report the development of a magnetic metamaterial composed of an array of unit cells featuring metallic helices. While different schemes have been reported to manipulate and enhance magnetic fields, from static to radio frequency (22–26), we propose an array of metallic helical unit cells with a collective resonance mode to interact with the magnetic field in MRI, thereby improving SNR. Previously, we have reported the use of metallic helices in their application to wireless communication and charging in a sensor system, enabling a high degree of magnetic field confinement within the helices (26), which is analogous to an electric field enhancement effect (27,28). Relevant to the work reported

herein is the fact that the magnetic field confinement also results in a marked degree of magnetic field enhancement in the vicinity of the helices. Therefore, by designing a metamaterial with unit cells composed of metallic helices, the metamaterial may inherit the capacity for field enhancement around a specific resonant mode. When applied to MRI, the resonant mode of the metamaterial may be excited by the radiofrequency (RF) magnetic fields employed during the MRI procedure, leading to a marked boost in RF field strength, ultimately leading to a dramatic increase in the SNR of MRI.

Results

Metamaterial structure design and analysis

The magnetic metamaterial reported herein is comprised of an array of metallic helices (Fig. 1), the coupling of which leads to a synergy and a bulk material property. The synergy of the metamaterial array yields the bulk property of a resonant mode in which the direction of the electric current induced by an applied RF field is identical in each unit cell. Upon excitation by an external RF field, the thusly-induced currents in the resonant mode lead to a dramatic enhancement of the RF field. With respect to MRI, when the frequency of the resonant mode approximates the resonance frequency of the MRI system, marked gains in both transmit and receive local RF magnetic fields (B_1+ and B_1-, respectively) are achieved, ultimately leading to gains in SNR.

In order to elucidate the determinants of the resonant mode of the metamaterial, electromagnetic theory can firstly be employed to define the equivalent self-inductance and mutual inductance of discrete unit cells as (29):

$$L_{ij} = \frac{\mu_0}{4\pi|I_iI_j|} \iint dr_i dr_j \frac{J(r_i) \cdot J(r_j)}{|r_i - r_j|}$$ (1)

where r_i and r_j are the integration elements along the path of the helix, I_i and I_j are the equivalent current in the helix, and J(r_i) and J(r_j) are the current densities (vectors) at r_i and r_j. Eq. 1 represents the self-inductance when i is equal to j and mutual inductance when i and j are different. At the resonant state, the amplitude of the current follows a sinusoidal profile along the path of the wire of the helix with a maximum (I_0) at the center and zero at the ends of the wire (29). Thusly, $I_{i,j} = I_0/\sqrt{2}$. The self-capacitance and mutual capacitance can be calculated by finding the inverse of the coefficients of the potential matrix (30) and, by employing electromagnetic theory, be expressed as:

$$P_{ij} = \frac{1}{4\varepsilon_0 \varepsilon_r |Q_iQ_j|} \iint dr_i dr_j \frac{\rho(r_i)\rho(r_j)}{|r_i - r_j|}$$ (2)

$$\begin{bmatrix} C_{11} & \cdots & C_{1m} \\ \vdots & \ddots & \vdots \\ C_{m1} & \cdots & C_{mm} \end{bmatrix} = \begin{bmatrix} P_{11} & \cdots & P_{1m} \\ \vdots & \ddots & \vdots \\ P_{m1} & \cdots & P_{mm} \end{bmatrix}^{-1}$$ (3)

in which Q_i and Q_j are the equivalent charge amounts in the helix and $\rho(r_i)$ and $\rho(r_j)$ are the charge densities (scalars) at r_i and r_j. The phase difference between the current and charge distribution is $\pi/2$ and, therefore, the maximal charge density is at the two ends of the helical wire (q_0) and zero at the middle of the wire. Taking into consideration the charge distribution, $Q_{i,j} = q_0 l_t \pi/\sqrt{2}$ where l_t is the total length of the wire wound to form the helix. The diagonal elements of the capacitance matrix yield the self-capacitance, while the remaining elements yield the corresponding mutual capacitance.

Upon implementation of the discrete unit cells into a metamaterial array, the effect of coupling must be considered, given its ultimate effect upon the resonant mode of the array. As the geometry of each unit cell is identical, the coupling coefficient of two adjacent helices may be expressed as $k = C_m/C + L_m/L$, in which C_m and L_m represent the mutual capacitance and mutual inductance, respectively, and C and L represent the self-capacitance and self-inductance, respectively. The total coupling coefficient (k), as well as the contributions from capacitance coupling (k_c) and inductance coupling (k_l) are plotted as a function of unit cell separation distance in Fig. 2. k_c and k_l are both negative and k_c is approximately 3-fold larger than k_l, demonstrating that a much larger contribution to the total coupling stems from the capacitance coupling between unit cells. In order to validate these theoretical results, numerical analyses were also conducted to derive the coupling coefficient and plotted in Fig. 2 (please see Supplementary Note 1 for further details).

Finally, due to the coupling between the discrete unit cells of the array, the resonant mode of the metamaterial may be derived by employing the coupled mode theory and solving the following equation system (31, 32):

$$\frac{da_n(t)}{dt} = -(j\omega_0 + \Gamma_n)a_n(t) + j\sum_{k=1}^{m,k \neq n} K_{kn}a_k(t), \quad n = 1, \cdots, m \tag{4}$$

in which $\omega_0 = 1/\sqrt{LC}$ presents the resonant angular frequency of a single helix, Γ_n is the intrinsic decay introduced by the material and radiation losses, K_{kn} is the coupling factor among unit cells and is related to the coupling coefficient k as $K_{kn} = k\omega_0/2$, and m is the total number of unit cells. The loss of each unit cell is omitted and only the coupling between adjacent unit cells is considered for simplicity to derive the resonant modes of the metamaterial (please see Supplementary Note 2 for further details). The eigenvalue represents the resonant frequency of the resonant mode and the corresponding eigenvector indicates the resonant strength and direction of each unit cell of the mode. By analyzing the resultant matrix, one can identify that the current direction in each unit cell is identical for the resonant mode with the highest resonant frequency, which will be referred to as the working mode.

The working mode of a metamaterial ordered as a 4×4 array as a function of unit cell separation distance was calculated, compared with simulation results, and illustrated in Fig. 3a. The degree of difference between the simulation results and the coupled mode theory increases as the coupling increases with decreasing separation distance, which is due to the weak coupling assumption of the coupled mode theory. However, as the separation distance increases, the theoretical results demonstrate a high degree of agreement with the simulation

results. The working modes for metamaterials composed of different numbers of unit cells are also illustrated in Fig. 3b with identical spacing between unit cells. The colors correspond to the resonant strength of each unit cell derived from the coupled mode theory. The unit cells at the center are found to resonate with the greatest strength, while the resonant strength decreases for the unit cells positioned along the periphery, thereby leading to larger degrees of magnetic field enhancement at the center of the metamaterials. For purposes of comparison, the relative magnetic field strength at the middle cross-section of a 4×4 metamaterial array is also simulated in CST Studio Suite 2017 and plotted as the inset at the bottom left corner in Fig. 3a, demonstrating a similar resonant strength pattern to that derived from the coupled mode theory.

Magnetic field distribution and field enhancement

Upon deployment of the metamaterials inside the bore of an MRI, by matching the frequency of the working mode to the working frequency of the MRI, the working mode can be excited by the RF magnetic field generated by the MRI (both transmit and receive RF magnetic fields; B_1+ and B_1-, respectively). The RF magnetic field leads to the induction of an AC voltage across the helix as $V = n S (dB_1+) / dt$. The impedance of the helix can be expressed as $Z_i = j\omega L + 1/j\omega C + R$, where L and C are the equivalent inductance and capacitance of the unit cell in the array, respectively, and R is the equivalent resistance, which is composed of the ohmic loss of the wire, as well as the dielectric loss of the scaffolding material. Therefore, the current inside the metallic helix can be calculated by $I = V / Z_i$. The induced magnetic field contains two components, both along the axial direction and the radial direction. Only the magnetic field component along the axial direction of the helix contributes to the magnetic field enhancement and can be calculated as (33):

$$B_Z = \frac{\mu_0 n I_0 a}{4\pi l} \int_{-l/2}^{l/2} \cos\left(\frac{\pi Z'}{l}\right) \int_0^{2\pi} \frac{a - \rho\cos(\varphi')}{\left[\rho^2 - 2a\rho\cos(\varphi') + a^2 + (z - z')^2\right]^{3/2}} d\varphi' dz' \quad (5)$$

in which I_0 is the amplitude of the current at the middle of the helix, n is the number of turns of the helix, a is the radius of the helix, l is the height of the helix, ρ and z are the polar coordinates of the target point, and $\cos(\pi z'/l)$ reflects the current distribution along the helix (please see Supplementary Note 3 for further details). The magnetic field enhancement ratio can be calculated by the summation of the magnetic field components (including the magnetic field generated by each unit cell and B_1+) and normalizing to B_1+, with the current strength in each unit cell indicated by the eigenvector of the coupled mode theory.

The magnetic field enhancement ratio at the mid-portion of the metamaterials along the axial direction is calculated and plotted as a function of distance from the metamaterial array in Fig. 4a. The magnetic field enhancement analysis is divided into three regions. Region A (shaded orange in Fig. 4a) is within the metamaterial and, although extremely high magnetic field enhancement is realized, this region is impractical for application to MRI imaging, as is considered herein. Region B (shaded yellow in Fig. 4a) extends from surface of the metamaterial to a distance where the direction of the magnetic field changes to the same direction as B_{1+} and the peak enhancement ratio outside the metamaterial is realized. Region C begins at and extends beyond the peak enhancement ratio distance and may be considered

the optimal region for placement of a sample to be imaged in MRI ('sample region'). The inset illustrates an extended analysis of the enhancement ratio of the sample region (Region C), indicating maximum magnetic field enhancement ratios of 5.84 and 6.01 for calculation and simulation results, respectively. Figure 4b depicts the simulated magnetic field distribution at the highlighted cross section of the inset. The field enhancement ratio along the white dashed line is also plotted in Fig. 4a demonstrating a high degree of agreement with the theoretical results. In addition to the decay of the magnetic field enhancement, the direction of the magnetic field in the vicinity of the metamaterials also varies at different locations, as shown in the Supplementary Figure 3. The magnetic field strength decay and direction variation leads to the gradient in the SNR enhancement, which will be discussed in detail below.

Finally, the magnetic field enhancement ratios of metamaterials configured with unit cells with different diameters were also theoretically modeled. As plotted in Fig. 4c, with the increase in the diameter, the peak enhancement ratio decreases accordingly and exhibits a relatively slower decay rate as a function of distance from the metamaterial array.

Noise analysis and SNR improvement

The expression for SNR in MRI, originally formulated by Hoult and Lauterbur (34, 35), is:

$$\text{SNR} \propto \frac{\omega^2 B_\text{c}}{\sqrt{r_\text{coil} + r_\text{sample}}} \tag{6}$$

where B_c is the magnetic field strength generated with unit current in the receiving coil and r_coil is the resistance of the receiving coil. r_sample is the equivalent resistance of the sample in the receiving coil, which can generate the same amount of heat with unit current as the heat generated by the induced current in the sample by the RF magnetic field (36, 37), as detailed in Supplementary Note 4. Through the application of the magnetic metamaterial, B_c may be enhanced due to the RF magnetic field enhancement detailed above, thereby increasing the signal. However, the introduction of the metamaterial also leads to an increase in the noise by increasing the total power dissipation, with a nearly 1.5-fold increase in the noise derived for our design (please see Supplementary Note 5 for further details).

If B_c is constant and r_sample is much larger than r_coil, the substitution of Eq. S18 in Supplementary Note 5 into Eq. 6 would seem to indicate that both signal and noise scale to an identical degree, thereby resulting in an absence of a net gain in SNR. Importantly, however, the introduction of the metamaterial results in the generation of a magnetic field gradient (see Fig. 4a). Therefore, as the degree of RF magnetic field enhancement along the sample in proximity to the metamaterial exceeds the increase in noise, significant gains in SNR are realized in Region C of Fig. 4a. Also notable is the capacity to tune the RF magnetic field enhancement gradients of the metamaterial through precise array design (such as unit cells with different diameters, see Fig. 4c), enabling the tailored application of metamaterials in MRI as a function of the tissue depth of interest, which is demonstrated below. Furthermore, it is noted that r_sample is proportional to the 4th order of the radius of the sample (please see Supplementary Note 5 for further details). Thus, when imaging small

parts (knees, wrists, etc.), r_{coil} dominates the noise and the degree of RF magnetic field enhancement approximates the ultimate gains in SNR.

Experimental MRI validation

Helices with identical geometries to the theoretical models employed in the analyses above were fabricated and employed for subsequent experimental validation. We employed 3D printing to fabricate hollow cylinders with grooves along their outer surface to serve as scaffolding (ABS P430). Subsequently, copper wires were wound along the 3D printed grooves in order to form the helices. Finally, the individual unit cells were aligned in an array in order to construct the complete magnetic metamaterial. Metamaterial arrays of two distinct geometries (4×4 array with unit cell diameter of 3 cm, 3×3 array with unit cell diameter of 5 cm) were fabricated and designed with a resonance frequency of 63.8 MHz, the operating frequency of the 1.5 T MRI employed herein. The two geometries of the metamaterials served to experimentally illustrate the capacity for tuning the RF magnetic field enhancement gradients (see Fig. 4c) such that the degree of SNR enhancement imaging may be optimized for more superficial (spine, for example) or deeper structures (liver, for example).

MRI experiments were performed in a clinical 1.5 T MRI and the birdcage body RF coil, located within the bore of the MRI system, was used for both RF transmission and reception (B_1+ and B_1-, respectively). The resonant frequency detuning of the body RF coil due to the presence of the metamaterials is trivial based on our simulation (from 64.14 MHz to 64.62 MHz) and may be readily compensated by the MRI system. Phantom MRI samples were prepared for imaging and composed of 2% agar gel in a 3D printed cubic mold with side length of 10 cm. Gradient echo imaging was performed both with and without the presence of the two distinct metamaterial arrays placed along the undersurface of the phantoms (top surface of the metamaterial array placed 2 cm from the bottom surface of the agar phantom; see Fig. 5a) (please see Methods for further details regarding MRI experiments). Given that the metamaterials led to enhancement of both transmission and reception RF energy (5.84 as shown in Fig. 4a), the transmission RF energy during the metamaterial-enhanced experiments was decreased such that, upon enhancement of B_1+, would approximate the transmission RF energy of control experiments employed for comparison of SNR. MRI images of the phantom with and without the presence of the 4×4 metamaterial array with unit cell diameter of 3 cm are shown in Figs. 5b and 5c, respectively, demonstrating a 4.2-fold increase in SNR. In addition, the degree of SNR enhancement achieved experimentally is compared to simulation and theoretical results in Fig. 5d, demonstrating a high degree of agreement.

Subsequently, a similar experimental approach was also conducted with metamaterials featuring a unit cell diameter of 5 cm in a 3×3 array. The MRI image in the presence of this metamaterial array is shown in Fig. 6a and a comparison of the experimental SNR enhancement ratios of the two distinct array geometries is shown in Fig. 6b. Notably, a lower peak SNR enhancement and slower decay rate as a function of distance from the metamaterial array is demonstrated with the larger unit cell diameter, similar to Fig. 4c.

Finally, MRI experiments were performed using a chicken leg to demonstrate the SNR enhancement capabilities of the magnetic metamaterial arrays. The experimental setup depicted in Fig. 5a was employed, along with identical MRI pulse sequences, but having replaced the phantom with a chicken leg. Images were acquired in the plane parallel to the top surface of the metamaterial array at distances of 2.25 cm (for Fig. 7a and 7b) and 2.50 cm (for Fig. 7c and 7d) from the array. In this case, when compared to images acquired in the absence of the metamaterial array (Fig. 7b and 7d), SNR enhancement of up to 3.6-fold was achieved (Fig. 7a and 7c) in the presence of the metamaterial. As a point of further consideration, currently, an alternative approach to increasing SNR commonly employed in clinical MRI is the use of signal averaging. In this case, all other experimental conditions remaining fixed, a 13.9-fold increase in scan time would be required to achieve a similar increase without the presented metamaterial in SNR through signal averaging, highlighting the potential utility of metamaterial-enhanced MRI.

Discussion

We have developed a magnetic metamaterial which, in its application to MRI, serves to enhance the RF magnetic fields and increase SNR. While the experimental validation reported herein was carried out using the body RF coil, the metamaterial may be readily employed in combination with surface RF receive coils. Alternatively, the combination of magnetic metamaterials with a body RF coil employed for both transmission and reception may be an avenue towards decreasing the technical complexity and cost of optimal surface RF receive coils. To enhance the practicality of this approach, future efforts may be directed at achieving a 'smart' metamaterial operating only during the RF reception phase of the MRI experiment. In this fashion, through either active or passive switching approaches, the metamaterial may be employed without any unwanted modifications to the MRI pulse sequences or safety concerns related to inappropriate RF energy deposition (maintaining specific absorption rates (SAR) within specified standard levels). Furthermore, optimization of the materials choices and array design may further improve the performance of the magnetic metamaterials, such as employing low-loss material and/or optimizing the configuration of the metamaterials to further increase the SNR boost. Finally, the physical footprint of the metamaterials may be significantly reduced through the use of high permittivity, low-loss scaffolding materials and insulating wire coatings, thereby allowing for flexible, sheet-like materials that may be readily used in combination or directly integrated with surface RF coils. While the focus of this work was on increasing SNR, an alternative consideration in its application to MRI would be to focus on the utility of the enhancement of the transmission RF energy that, for example, may lead to lower RF power amplifier hardware requirements. In summary, we report the development of magnetic metamaterials and validate their application to MRI in order to improve the SNR, a fundamental performance metric that may be leveraged to drive improvements in the overall acquisition quality, from image resolution to the efficiency of image acquisition.

Methods

Geometry of the metamaterial structure

A 4×4 metamaterial array, as shown in Fig. 1, was employed to conduct the theoretical analyses. The geometries of each helix were 32 mm, 15 mm, 0.28 mm, and 25 for height, radius, wire diameter and number of turns, respectively. The wires of the helices were composed of copper and the permittivity of the scaffolding core material was assumed as $2\times$ (1+0.03j) (ABS P430). An additional 3×3 array was employed during the MRI experiments in order to demonstrate the manipulation of the field enhancement gradient and featured geometries of 30 mm, 25 mm, 0.28 mm, and 12 for height, radius, wire diameter and number of turns, respectively. The resonant frequencies of the metamaterial were tuned and measured with a network analyzer by utilizing a coupling loop in order to match the working frequency of a 1.5 T MRI at 63.8 MHz.

Magnetic resonance imaging validation

All MRI experiments were performed in a 1.5 T clinical MRI system (Intera, Philips Healthcare). A gradient echo pulse sequence (TE = 13.81 ms, TR = 1600 ms) was employed throughout. Given that the metamaterials lead to an enhancement of transmission RF energy, the transmission energy was reduced during the MRI experiments in the presence of the metamaterial array. To this end, the flip angle of the gradient echo image acquisition was decreased to 18°, given the expected transmission RF energy increase of ~5-fold (see Fig. 4). In the absence of the metamaterial arrays, a 90° flip angle was employed, allowing for a comparison of MRI SNR with and without the presence of the metamaterials while mitigating the confounding effect of RF transmission energy enhancement.

Supplementary Material

Refer to Web version on PubMed Central for supplementary material.

Acknowledgments:

References:

1. Owen RS & Wehrli FW, Predictability of SNR and reader preference in clinical MR imaging. Magn. Reson. Imaging 8, 737–745 (1990). [PubMed: 2266800]

2. Kuhl CK et al. Acute and subacute ischemic stroke at high-field-strength (3.0-T) diffusion-weighted MR imaging: intraindividual comparative study. Radiology 234, 509–516 (2005). [PubMed: 15601894]

3. Fischbach F, Muller M & Bruhn H Magnetic resonance imaging of the cranial nerves in the posterior fossa: a comparative study of t2-weighted spin-echo sequences at 1.5 and 3.0 tesla. Acta Radiol. 49, 358–363 (2008). [PubMed: 18365827]

4. Fischbach F et al. Magnetic resonance imaging of hyaline cartilage defects at 1.5T and 3.0T: comparison of medium T2-weighted fast spin echo, T1-weighted two-dimensional and three-dimensional gradient echo pulse sequences. Acta Radiol. 46, 67–73 (2005). [PubMed: 15841742]

5. Michaely HJ et al. Intraindividual comparison of high-spatial-resolution abdominal MR angiography at 1.5T and 3.0T: Initial experience. Radiology 244, 907–913 (2007). [PubMed: 17709837]

6. Stahl R et al. Assessment of cartilage-dedicated sequences at ultra-high-field MRI: comparison of imaging performance and diagnostic confidence between 3.0 and 7.0 T with respect to osteoarthritis-induced changes at the knee joint. Skeletal Radiol. 38, 771–783 (2009). [PubMed: 19294379]

7. Mazaheri Y et al. Image artifacts on prostate diffusion-weighted magnetic resonance imaging: trade-offs at 1.5 Tesla and 3.0 Tesla. Acad. Radiol 20, 1041–1047 (2013). [PubMed: 23830610]

8. Versluis MJ et al. Subject tolerance of 7 T MRI examinations. J. Magn. Reson. Imaging 38, 722–725 (2013). [PubMed: 23150466]

9. Kollia K et al. First clinical study on ultra-high-field MR imaging in patients with multiple sclerosis: comparison of 1.5T and 7T. AJNR Am. J. Neuroradiol 30, 699–702 (2009). [PubMed: 19147714]

10. Porter JR, Wright SM & Reykowski AA 16-element phased-array head coil. Magn. Reson. Med 40, 272–279 (1998). [PubMed: 9702709]

11. Sengupta S, et al. A specialized multi-transmit head coil for high resolution fMRI of the human visual cortex at 7T. PLoS One 11, e0165418 (2016). [PubMed: 27911950]

12. Lustig M, Donoho D & Pauly JM Sparse MRI: The application of compressed sensing for rapid MR imaging. Magn. Reson. Med 58, 1182–1195 (2007). [PubMed: 17969013]

13. Veselago VG The electrodynamics of substances with simultaneously negative values of ε and μ. Soviet Physics Uspekhi 10, 509–518 (1968).

14. Pendry JB et al. Magnetism from conductors and enhanced nonlinear phenomena. IEEE Trans. Microw. Theory Techn 47, 2075–2084 (1999).

15. Shelby RA Smith DR & Schultz S, Experimental verification of a negative index of refraction. Science 292, 77–79 (2001). [PubMed: 11292865]

16. Wiltshire MC et al. Microstructured magnetic materials for RF flux guides in magnetic resonance imaging. Science 291, 849–851 (2001). [PubMed: 11157159]

17. Freire MJ, Marques R & Jelinek L Experimental demonstration of a $\mu=-1$ metamaterial lens for magnetic resonance imaging. Appl. Phys. Lett 93, 231108 (2008).

18. Freire MJ, Jelinek L, Marques R & Lapine M On the applications of $\mu=-1$ metamaterial lenses for magnetic resonance imaging. J. Magn. Reson 203, 81–90 (2010). [PubMed: 20036589]

19. Syms RRA, Floume T, Young IR, Solymar L & Reab M Flexible magnetoinductive ring MRI detector: Design for invariant nearest-neighbour coupling. Metamaterials 4, 1–14 (2010).

20. Radua X, Garrayb D & Craeyea C Toward a wire medium endoscope for MRI imaging. Metamaterials 3, 90–99 (2009).

21. Slobozhanyuk AP et al., Enhancement of Magnetic Resonance Imaging with Metasurfaces. Adv. Mater 28, 1832–1838 (2016). [PubMed: 26754827]

22. Oh J et al., Detection of magnetic nanoparticles in tissue using magneto-motive ultrasound, Nanotechnology, 17, 4183–4190 (2006). [PubMed: 21727557]

23. Park J-K et al., 3D field phase-space control in tokamak plasmas, Nat. Phys 14, 1223–1228 (2018).

24. Chabalko MJ, Besnoff J & Ricketts DS Magnetic field enhancement in wireless power with metamaterials and magnetic resonant couplers, IEEE Antennas Wirel. Propag. Lett 15, 452–455 (2016).

25. Sun J et al., Experimental demonstration of anomalous field enhancement in all-dielectric transition magnetic metamaterials, Sci. Rep 5, 16154 (2015). [PubMed: 26531855]

26. Duan G, Zhao X & Zhang X A magnetically coupled communication and charging platform for microsensors. J. Microelectromech. Syst 26, 1099–1109 (2017).

27. Valagiannopoulos CA & Sihvola A Improving the electrostatic field concentration in a negative-permittivity wedge with a grounded "bowtie" configuration, Radio Sci. 48, 316–325 (2013).

28. Bionta MR et al., Wavelength and shape dependent strong-field photoemission from silver nanotip, New J. Phys 18, 103010 (2016).

29. Kurs A et al. Wireless power transfer via strongly coupled magnetic resonances. Science 317, 83–86 (2007). [PubMed: 17556549]

30. Huray PG Maxwell's Equation. John Wiley & Sons, New Jersey (2010).

31. Haus HA Waves and Fields in Optoelectronics Prentice-Hall, New Jersey (1984).

32. Karalis A, Joannopoulos J, & Soljacic DM Efficient wireless non-radiative mid-range energy transfer. Ann. Phys 323, 34–48 (2008).

33. Derby N & Olbert S Cylindrical magnets and ideal solenoids. Am. J. Phys 78, 229–235 (2010).

34. Hayes CE & Axel L Noise performance of surface coils for magnetic resonance imaging at 1.5T. Med. Phys 12, 604–607 (1985). [PubMed: 4046995]

35. Hoult DI & Richards RE The signal-to-noise ratio of the nuclear magnetic resonance experiment. J. Magn. Reson 24, 71–85 (1976).

36. Hong JS & Lancaster MJ Microstrip Filters for RF/microwave Applications, John Wiley & Sons, New Jersey (2001).

37. Hoult DI The sensitivity of the Zeugmatographic experiment involving human samples. J. Magn. Reson 34, 425–433 (1979).
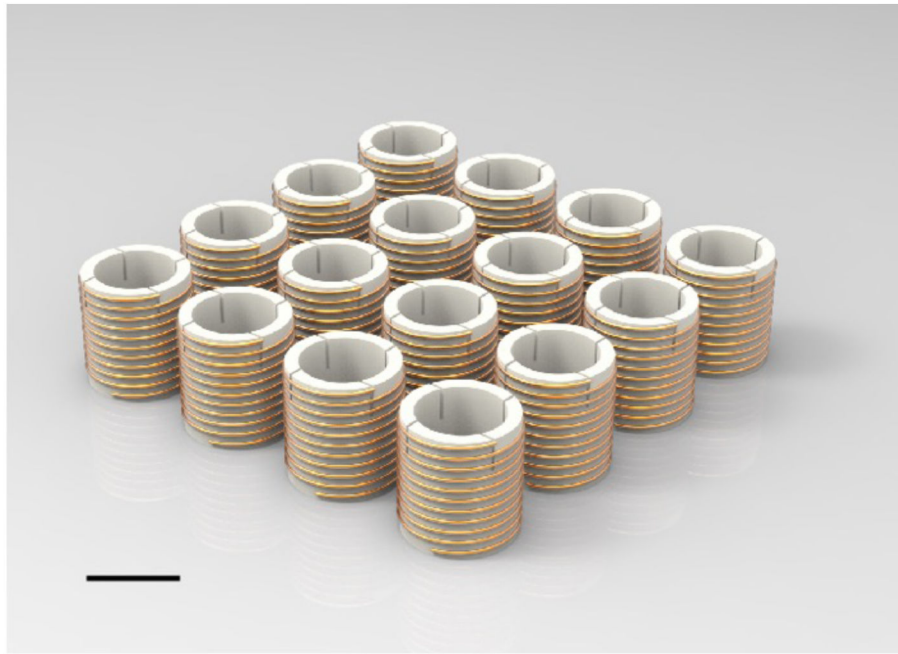
Fig. 1. Schematic of the magnetic metamaterial.
The metamaterial array composes unit cells featuring metallic helices, which are made of copper wiring with central polymeric scaffolding. Scale bar is 3 cm. (dimension included for scale and employed in subsequent analyses, see Methods).
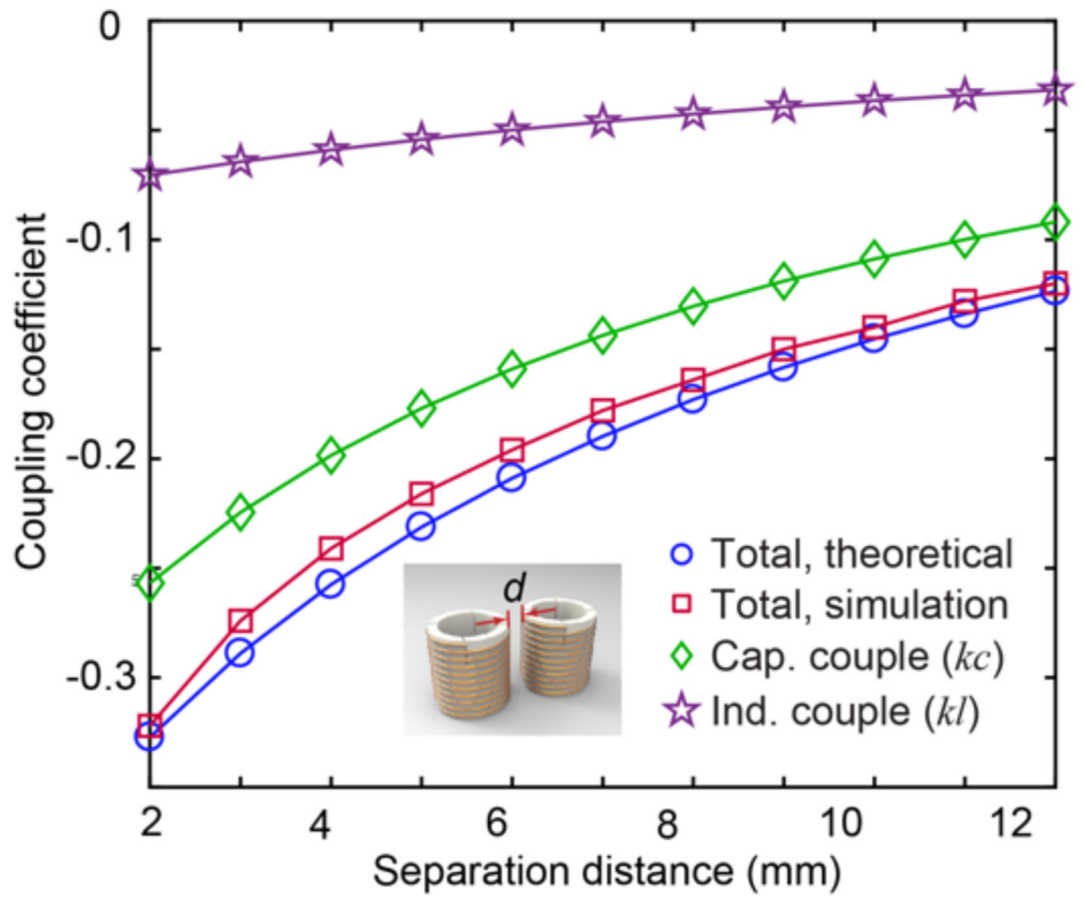
Fig. 2. Coupling coefficients between adjacent unit cells.
Coupling coefficients as a function of unit cell separation distance derived from both theoretical and numerical analyses.
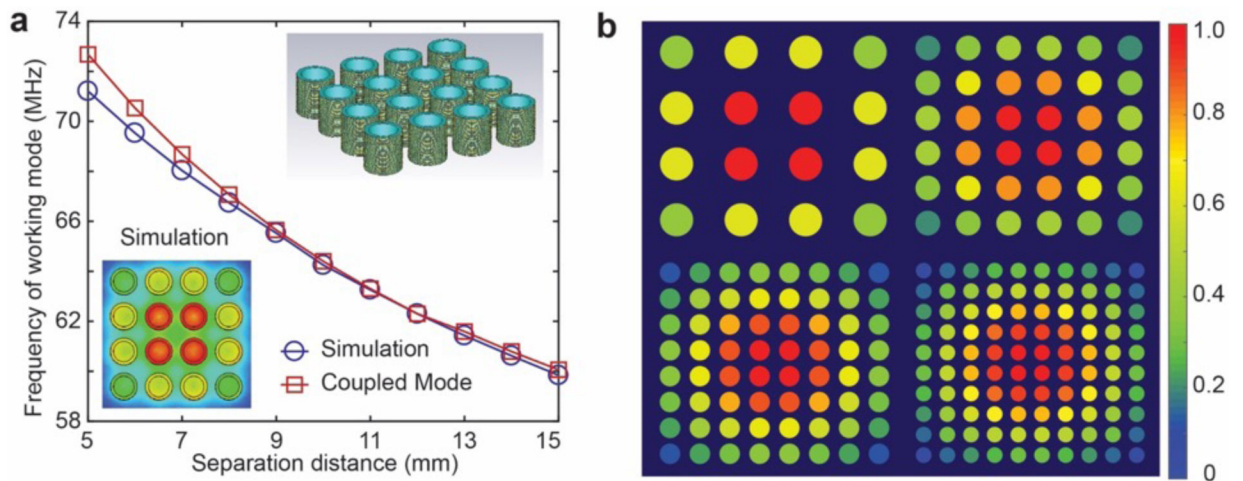
Fig. 3. Resonant mode of the metamaterials.
(**a**) The frequency of the working mode of the metamaterial as a function of separation distance of unit cells. Inset on the bottom left plots the simulated magnetic field at the middle cross section of the metamaterials. Inset on the top right depicts the model used for simulation. (**b**) The resonant strength derived from the coupled mode theory for metamaterials with 4×4, 6×6, 8×8, and 10×10 arrays. The resonant strength is normalized to the maximum value.
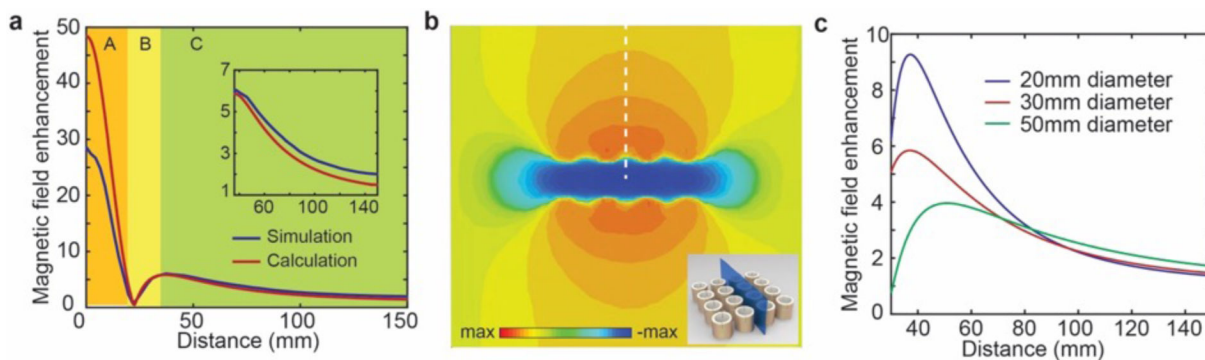
**Fig. 4. Magnetic field enhancement ratio of the metamaterials.**
(**a**) Magnetic field enhancement ratio as a function of distance from the center of the metamaterial array (along the white dashed line in (**b**)) with simulation and calculation results in blue and red. Regions A, B, and C correspond to the regions within the metamaterial array, the region extending from the surface of the metamaterial to the peak enhancement ratio, and the 'sample region' beyond the peak enhancement, respectively. The inset illustrates an extended plot of Region C ('sample region'). (**b**) The magnetic field strength along the axial direction distributed at the cross section depicted as the blue rectangle in the inset. (**c**) The theoretical magnetic field enhancement ratio of metamaterials with unit cells with different diameters.
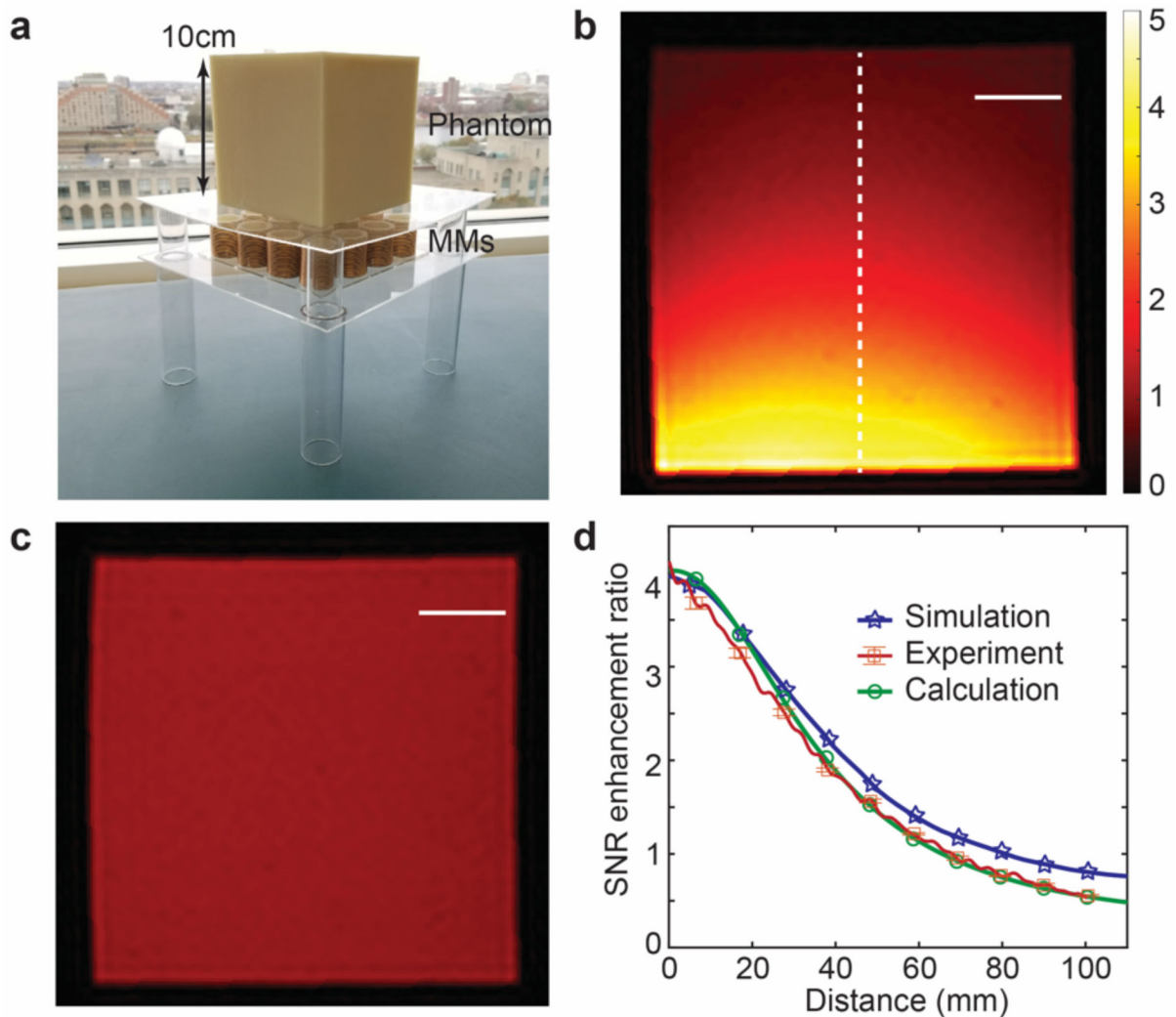
**Fig. 5. Experimental results with and without metamaterials.**
(**a**) Experimental setup of metamaterial array beneath 3D printed magnetic resonance imaging (MRI) phantom containing 2% agar gel. (**b**) MRI image in presence of 4 × 4 metamaterial array with unit cell diameter of 3 cm (transmission radio frequency (RF) power of MRI experiment reduced, see Methods; the dashed line used for comparison of signal-to-noise ratio (SNR) in (**d**)). (**c**) Control MRI image in the absence of metamaterial array (transmission RF energy not reduced, see Methods). Scale bars correspond to 2 cm in (b) and (c). (**d**) Comparison of SNR enhancement ratios of experimental, simulation, and calculation results. The bars for experimental results show the standard deviation of the measured SNR enhancement ratio.
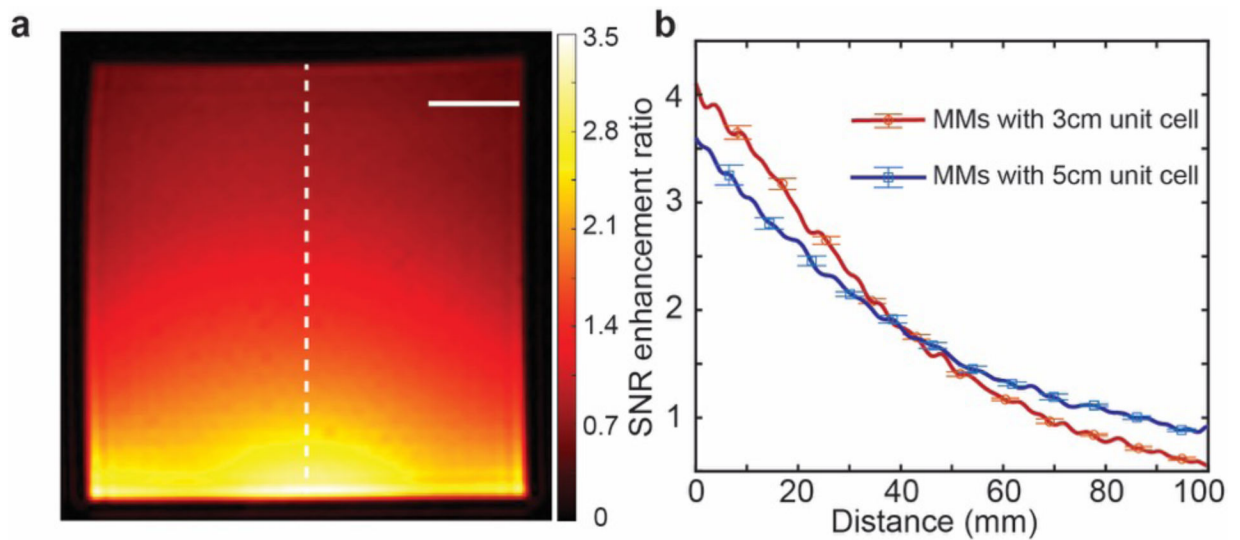
Fig. 6. Experimental results with larger unit cells.
(**a**) Magnetic resonance imaging (MRI) image in presence of 3×3 metamaterial array with diameter of 5 cm (transmission radio frequency (RF) power of MRI experiment reduced, see Methods; the dashed line used for comparison of signal-to-noise ratio (SNR) in (**b**)). The scale bar is 2 cm. (**b**) Comparison of SNR enhancement ratios of metamaterial arrays with distinct unit cell diameters. The larger unit cell (red line) exhibits lower peak SNR enhancement and slower decay rate as a function of distance from the top surface of the metamaterial array. The bars for experimental results show the standard deviation of the measured SNR enhancement ratio.
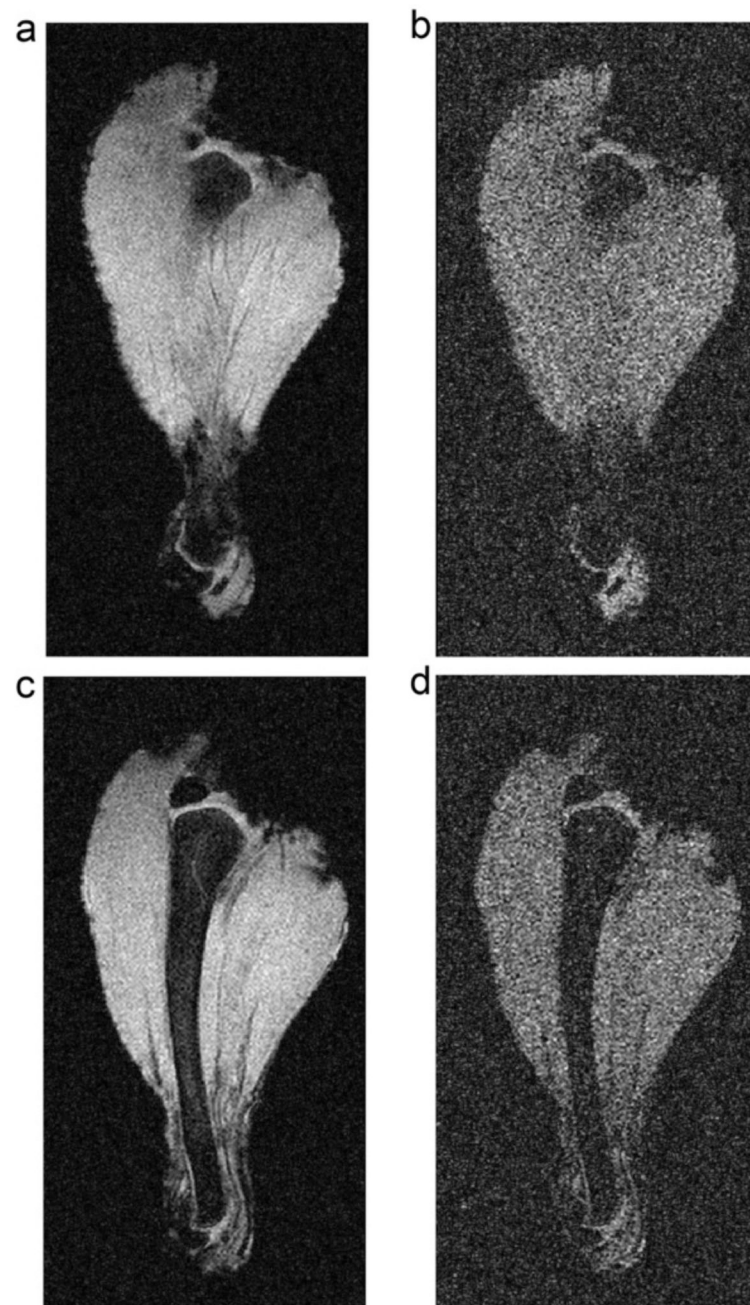
Fig. 7. MRI scan of chicken leg.
Images acquired 2.25 cm (**a**), (**b**) and 2.50 cm (**c**), (**d**), from the top surface of the metamaterial array. Images (**a**) and (**c**) are acquired in the presence of the metamaterial array while images (**b**) and (**d**) are acquired in the absence of the metamaterial array. All other experimental conditions remain fixed between scans.